



Lepton flavor violating decays $l_j \rightarrow l_i \gamma$ in the $U(1)_X$ SSM model within the mass insertion approximation

Tong-Tong Wang^{1,2,a}, Shu-Min Zhao^{1,2,b}, Jian-Fei Zhang^{1,2,c}, Xing-Xing Dong^{1,2,d}, Tai-Fu Feng^{1,2,3,e}

¹ Department of Physics, Hebei University, Baoding 071002, China

² Key Laboratory of High-precision Computation and Application of Quantum Field Theory of Hebei Province, Baoding 071002, China

³ Department of Physics, Chongqing University, Chongqing 401331, China

Received: 22 May 2022 / Accepted: 18 July 2022 / Published online: 25 July 2022
© The Author(s) 2022

Abstract Three singlet new Higgs superfields and right-handed neutrinos are added to MSSM to obtain $U(1)_X$ SSM model. Its local gauge group is $SU(3)_C \times SU(2)_L \times U(1)_Y \times U(1)_X$. In the framework of $U(1)_X$ SSM, we study muon anomalous magnetic moment and lepton flavor violating decays $l_j \rightarrow l_i \gamma$ ($j = 2, 3; i = 1, 2$) within the mass insertion approximation (MIA). Through the MIA method, we can find the parameters that directly affect the analytical result of the lepton flavor violating decays $l_j \rightarrow l_i \gamma$, which make our work more convenient. We want to provide a set of simple analytic formulas for the form factors and the associated effective vertices, that may be very useful for future phenomenological studies of the lepton flavor violating decays. According to the accuracy of the numerical results which the influence of different sensitive parameters, we come to the conclusion that the non-diagonal elements which correspond to the generations of the initial lepton and final lepton are main sensitive parameters and lepton flavor violation (LFV) sources. This work can provide a clear signal of new physics (NP).

1 Introduction

Lepton has unitary matrix similar to Cabibbo–Kobayashi–Maskawa (CKM) mixed matrix. The breaking theory of electric weak symmetry and neutrino oscillation experiment show that lepton flavor violation (LFV) exists both theoretically and experimentally [1–3]. The standard model (SM) is already a mature theory. However, the lepton number is

conserved in the SM, so there is no LFV process in the SM [4]. Through research, it is necessary to expand the SM. Any sign of LFV can be regarded as evidence of the existence of new physics (NP) [5].

Physicists have extended SM and obtained a large number of extended models, among which the minimum supersymmetric standard model (MSSM) is the most concerned model. However, it is gradually found that MSSM also has problems: μ problem [6] and zero mass neutrinos [7]. To solve these problems, we pay attention to the $U(1)$ expansions of MSSM. We extend the MSSM with $U(1)_X$ gauge group, whose symmetry group is $SU(3)_C \times SU(2)_L \times U(1)_Y \times U(1)_X$ [8–10]. It adds three Higgs singlet superfields and right-handed neutrino superfields beyond MSSM [11]. There are five neutral CP-even Higgs component fields in the model, which come from two Higgs doublets and three Higgs singlets respectively. Therefore, the mass mixing matrix is 5×5 , and the 125.1 GeV Higgs particle [12, 13] corresponds to the lightest mass eigenstate.

To improve the corrections to LFV processes of $l_j \rightarrow l_i \gamma$, people discuss different SM extended models [14], for example minimal R-symmetric supersymmetric standard model [15], MSSM extension with gauged baryon and lepton numbers [16], SM extension with a hidden $U(1)_X$ gauged symmetry [17] and lepton numbers and supersymmetric low-scale seesaw models [18]. It is worth noting that in our previous work, we have studied lepton flavor violating decays $l_j \rightarrow l_i \gamma$ in the $U(1)_X$ SSM model [19]. The above works and most of the research on LFV are studied with the mass eigenstate method. Using this method to find sensitive parameters is often not intuitive and clear enough, which depends on the mass eigenstates of the particles and rotation matrices. It will lead us to pay too much attention to many unimportant parameters. Now we use a novel calculation method called as mass insertion approximation (MIA) [20–23], which uses the electroweak interaction eigenstate and treats perturba-

^a e-mail: wtt961018@163.com (corresponding author)

^b e-mail: zhaosm@hbu.edu.cn

^c e-mail: zjf09@hbu.edu.cn

^d e-mail: dongxx@hbu.edu.cn

^e e-mail: fengtf@hbu.edu.cn

tively the mass insertions changing slepton flavor. By means of mass insertions inside the propagators of the electroweak interaction sleptons eigenstates, at the analytical level, we can find many parameters that have direct impact on LFV. It is worth noting that these parameters are considered between all possible flavor blends among SUSY partner of leptons, in which their particular origin has no assumption and is independent of the model [21]. In addition, the MIA method has been applied to other works related to LFV, including the $h, H, A \rightarrow \tau\mu$ decays induced from SUSY loops [21], effective lepton flavor violating $H\ell_i\ell_j$ vertex from right-handed neutrinos [22], one-loop effective LFV Zl_kl_m vertex from heavy neutrinos [23] and so on. This method provides very simple and intuitive analytical formula, and is also clear about the changes of the main parameters affecting lepton taste destruction, which provides a new idea for other work of LFV in the future.

In the process of LFV, because the mass of τ lepton is much greater than μ and e , there are more LFV decay channels [24]. The decay processes of $l_j \rightarrow l_i\gamma$ are the most interesting. This work is to study the LFV of the $l_j \rightarrow l_i\gamma$ processes under the $U(1)_X$ S SM model. The effects of different reasonable parameter spaces on the branching ratio $Br(l_j \rightarrow l_i\gamma)$ are compared. The latest upper limits on the LFV branching ratio of $\mu \rightarrow e\gamma, \tau \rightarrow \mu\gamma$ and $\tau \rightarrow e\gamma$ at 90% confidence level (CL) [25] are

$$Br(\mu \rightarrow e\gamma) < 4.2 \times 10^{-13}, \quad Br(\tau \rightarrow \mu\gamma) < 4.4 \times 10^{-8}, \\ Br(\tau \rightarrow e\gamma) < 3.3 \times 10^{-8}. \tag{1}$$

The paper is organized as follows. In Sect. 2, we mainly introduce the $U(1)_X$ S SM including its superpotential and the general soft breaking terms. In Sect. 3, we give analytic expressions for muon anomalous magnetic moment and the branching ratios of $l_j \rightarrow l_i\gamma$ decays in the $U(1)_X$ S SM. In Sect. 4, we give the numerical analysis, and the summary is given in Sect. 5.

2 The $U(1)_X$ S SM

$U(1)_X$ S SM is the U(1) extension of MSSM, whose local gauge group is $SU(3)_C \otimes SU(2)_L \otimes U(1)_Y \otimes U(1)_X$ [7,20,26]. On the basis of MSSM, $U(1)_X$ S SM has new superfields such as three Higgs singlets $\hat{\eta}, \hat{\bar{\eta}}, \hat{S}$ and right-handed neutrinos $\hat{\nu}_i$. Through the seesaw mechanism, light neutrinos obtain tiny masses at the tree level. The neutral CP-even parts of $H_u, H_d, \eta, \bar{\eta}$ and S mix together and form a 5×5 mass squared matrix, whose lightest mass eigenvalue corresponds to the lightest CP-even Higgs. The particle content and charge assignments for $U(1)_X$ S SM can be found in our previous work [7]. To get 125.1 GeV Higgs mass [27,28], the loop corrections should be taken into account.

The sneutrinos are parted into CP-even sneutrinos and CP-odd sneutrinos, and their mass squared matrixes are both extended to 6×6 .

In $U(1)_X$ S SM, the concrete form of the superpotential is:

$$W = l_W \hat{S} + \mu \hat{H}_u \hat{H}_d + M_S \hat{S} \hat{S} - Y_d \hat{d} \hat{Q} \hat{H}_d - Y_e \hat{e} \hat{L} \hat{H}_d \\ + \lambda_H \hat{S} \hat{H}_u \hat{H}_d + \lambda_C \hat{S} \hat{\eta} \hat{\bar{\eta}} + \frac{\kappa}{3} \hat{S} \hat{S} \hat{S} \\ + Y_u \hat{u} \hat{Q} \hat{H}_u + Y_X \hat{\nu} \hat{\eta} \hat{\bar{\nu}} + Y_\nu \hat{\nu} \hat{L} \hat{H}_\nu. \tag{2}$$

We collect the explicit forms of two Higgs doublets and three Higgs singlets here

$$H_u = \begin{pmatrix} H_u^+ \\ \frac{1}{\sqrt{2}}(v_u + H_u^0 + iP_u^0) \end{pmatrix}, \\ H_d = \begin{pmatrix} \frac{1}{\sqrt{2}}(v_d + H_d^0 + iP_d^0) \\ H_d^- \end{pmatrix}, \\ \eta = \frac{1}{\sqrt{2}}(v_\eta + \phi_\eta^0 + iP_\eta^0), \\ \bar{\eta} = \frac{1}{\sqrt{2}}(v_{\bar{\eta}} + \phi_{\bar{\eta}}^0 + iP_{\bar{\eta}}^0), \\ S = \frac{1}{\sqrt{2}}(v_S + \phi_S^0 + iP_S^0). \tag{3}$$

The vacuum expectation values(VEVs) of the Higgs superfields $H_u, H_d, \eta, \bar{\eta}$ and S are denoted by $v_u, v_d, v_\eta, v_{\bar{\eta}}$ and v_S respectively. Two angles are defined as $\tan \beta = v_u/v_d$ and $\tan \beta_\eta = v_{\bar{\eta}}/v_\eta$.

The soft SUSY breaking terms of this model are shown as

$$\mathcal{L}_{soft} = \mathcal{L}_{soft}^{MSSM} - B_S S^2 - L_S S \\ - \frac{T_k}{3} S^3 - T_{\lambda_C} S \eta \bar{\eta} + \epsilon_{ij} T_{\lambda_H} S H_d^i H_u^j \\ - T_X^{IJ} \bar{\eta} \tilde{\nu}_R^{*I} \tilde{\nu}_R^{*J} + \epsilon_{ij} T_v^{IJ} H_u^i \tilde{\nu}_R^{*I} \tilde{L}_j^J - m_\eta^2 |\eta|^2 - m_{\bar{\eta}}^2 |\bar{\eta}|^2 - m_S^2 S^2 \\ - (m_{\tilde{\nu}_R}^2)^{IJ} \tilde{\nu}_R^{*I} \tilde{\nu}_R^J - \frac{1}{2} (M_X \lambda_X^2 + 2M_{BB'} \lambda_B \lambda_{\bar{X}}) + h.c. \tag{4}$$

We have proven that $U(1)_X$ S SM is anomaly free in our previous work [26]. Two Abelian groups $U(1)_Y$ and $U(1)_X$ produce a new effect called as the gauge kinetic mixing in the $U(1)_X$ S SM, which is MSSM never before.

In general, the covariant derivatives of $U(1)_X$ S SM can be written as [29–32]

$$D_\mu = \partial_\mu - i(Y, X) \begin{pmatrix} g_Y & g'_{YX} \\ g'_{XY} & g'_X \end{pmatrix} \begin{pmatrix} A_\mu^Y \\ A_\mu^X \end{pmatrix}, \tag{5}$$

with A_μ^Y and A_μ^X representing the gauge fields of $U(1)_Y$ and $U(1)_X$ respectively.

Under the condition that the two Abelian gauge groups are unbroken, we use the rotation matrix R [29,31,32] to perform a change of the basis

$$D_\mu = \partial_\mu - i(Y^Y, Y^X) \begin{pmatrix} g_Y & g'_{YX} \\ g'_{XY} & g'_X \end{pmatrix} R^T R \begin{pmatrix} A'^Y_\mu \\ A'^X_\mu \end{pmatrix}, \tag{6}$$

with the redefinitions

$$\begin{pmatrix} g_Y & g'_{YX} \\ g'_{XY} & g'_X \end{pmatrix} R^T = \begin{pmatrix} g_1 & g_{YX} \\ 0 & g_X \end{pmatrix} \text{ and} \\ R \begin{pmatrix} A'^Y_\mu \\ A'^X_\mu \end{pmatrix} = \begin{pmatrix} A^Y_\mu \\ A^X_\mu \end{pmatrix}. \tag{7}$$

Then the covariant derivatives of $U(1)_X$ SSM are changed as

$$D_\mu = \partial_\mu - i(Y^Y, Y^X) \begin{pmatrix} g_1 & g_{YX} \\ 0 & g_X \end{pmatrix} \begin{pmatrix} A^Y_\mu \\ A^X_\mu \end{pmatrix}. \tag{8}$$

At the tree level, three neutral gauge bosons A^X_μ, A^Y_μ and V^3_μ mix together, whose mass matrix is shown in the basis $(A^Y_\mu, V^3_\mu, A^X_\mu)$ [20]

$$\begin{pmatrix} \frac{1}{8}g_1^2v^2 & -\frac{1}{8}g_1g_2v^2 & \frac{1}{8}g_1(g_{YX} + g_X)v^2 \\ -\frac{1}{8}g_1g_2v^2 & \frac{1}{8}g_2^2v^2 & -\frac{1}{8}g_2g_{YX}v^2 \\ \frac{1}{8}g_1(g_{YX} + g_X)v^2 & -\frac{1}{8}g_2(g_{YX} + g_X)v^2 & \frac{1}{8}(g_{YX} + g_X)^2v^2 + \frac{1}{8}g_X^2\xi^2 \end{pmatrix}, \tag{9}$$

with $v^2 = v_u^2 + v_d^2$ and $\xi^2 = v_\eta^2 + v_\rho^2$.

We use two mixing angles θ_W and θ'_W to get mass eigenvalues of the matrix in Eq. (9). θ_W is the Weinberg angle and the new mixing angle θ'_W is defined from the following formula

$$\sin^2 \theta'_W = \frac{1}{2} - \frac{[(g_{YX} + g_X)^2 - g_1^2 - g_2^2]v^2 + 4g_X^2\xi^2}{2\sqrt{[(g_{YX} + g_X)^2 + g_1^2 + g_2^2]v^4 + 8g_X^2[(g_{YX} + g_X)^2 - g_1^2 - g_2^2]v^2\xi^2 + 16g_X^4\xi^4}}. \tag{10}$$

It appears in the couplings involving Z and Z' . The exact eigenvalues of Eq. (9) are deduced [20]

$$m_\gamma^2 = 0, \\ m_{Z,Z'}^2 = \frac{1}{8}([g_1^2 + g_2^2 + (g_{YX} + g_X)^2]v^2 + 4g_X^2\xi^2 \mp \sqrt{[g_1^2 + g_2^2 + (g_{YX} + g_X)^2]v^4 + 8[(g_{YX} + g_X)^2 - g_1^2 - g_2^2]g_X^2v^2\xi^2 + 16g_X^4\xi^4}). \tag{11}$$

The used mass matrixes can be found in the work [7, 19]. Here, we show some needed couplings in this model. We deduce the vertexes of $\bar{l}_i - \chi_j^- - \tilde{\nu}_k^R(\tilde{\nu}_k^l)$

$$\mathcal{L}_{\bar{l}_i\chi_j^-\tilde{\nu}_k^R} = \frac{1}{\sqrt{2}}\bar{l}_i \left\{ \tilde{\nu}_L^R Y_l^i P_L \tilde{H}_1^- - g_2 \tilde{\nu}_L^R P_R \tilde{W}^- \right\}, \\ \mathcal{L}_{\bar{l}_i\chi_j^-\tilde{\nu}_k^l} = \frac{i}{\sqrt{2}}\bar{l}_i \left\{ \tilde{\nu}_L^l Y_l^i P_L \tilde{H}_1^- - g_2 \tilde{\nu}_L^l P_R \tilde{W}^- \right\}. \tag{12}$$

We deduce the vertex couplings of neutralino-lepton-slepton

$$\mathcal{L}_{\tilde{\chi}^0 i \tilde{L}} = \left\{ \left(\frac{1}{\sqrt{2}}(g_1 \lambda_{\tilde{B}} + g_2 \tilde{W}^0 + g_{YX} \lambda_{\tilde{X}}) \tilde{L}^L - \tilde{H}_d^0 Y_l^j \tilde{L}^R \right) P_L - \left[\frac{1}{\sqrt{2}}(2g_1 \lambda_{\tilde{B}} + (2g_{YX} + g_X) \lambda_{\tilde{X}}) \tilde{L}^R + \tilde{H}_d^0 Y_l^j \tilde{L}^L \right] P_R \right\} l_j. \tag{13}$$

3 Formulation

In this section, we study the LFV of the $l_j \rightarrow l_i \gamma$ ($j = 2, 3; i = 1, 2$) and muon anomalous magnetic moment under the $U(1)_X$ SSM model [16] with the MIA. The simplified form is discussed.

3.1 Using MIA to calculate $l_j \rightarrow l_i \gamma$ in $U(1)_X$ SSM model

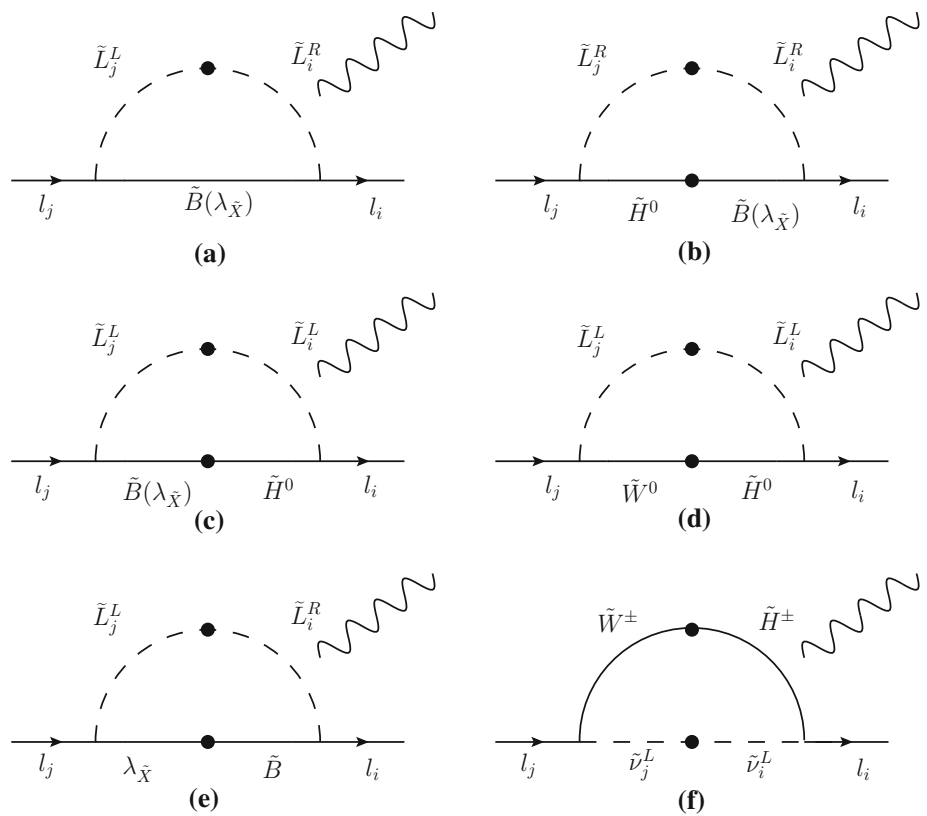
If the external lepton is on shell, the amplitude of $l_j \rightarrow l_i \gamma$ is

$$\mathcal{M} = e\varepsilon^\mu \bar{u}_i(p+q)[q^2 \gamma_\mu (C_1^L P_L + C_1^R P_R) + m_{l_j} i \sigma_{\mu\nu} q^\nu (C_2^L P_L + C_2^R P_R)] u_j(p), \tag{14}$$

where p is the injecting lepton momentum, q is the photon momentum, and m_{l_j} is the mass of the j th generation charged lepton. $\bar{u}_i(p)$ and $u_j(p)$ are the wave functions for the external leptons. The final Wilson coefficients $C_1^L, C_1^R, C_2^L, C_2^R$ are obtained from the sum of these diagrams' amplitudes.

The Feynman diagrams of $l_j \rightarrow l_i \gamma$ under the $U(1)_X$ SSM model are obtained by MIA [33] in Fig. 1. The sneutrinos are

Fig. 1 Feynman diagrams for $l_j \rightarrow l_i \gamma$ in the MIA



disparted into CP-even sneutrinos $\tilde{\nu}^R$ and CP-odd sneutrinos $\tilde{\nu}^L$. After our analysis, in Fig. 1f since right-handed sneutrinos are strongly depressed by Y_ν , the situation of right-handed sneutrinos here is neglected. In other words, there are only two cases of left-handed CP-even sneutrinos $\tilde{\nu}_L^R$ and left-handed CP-odd sneutrinos $\tilde{\nu}_L^L$ in Fig. 1f. In order to more directly express the influencing factors of LFV of $l_j \rightarrow l_i \gamma$, we use $C_2^f = C_2^{Lf} = C_2^{Rf}$ ($f = 1 \dots 6$) to express the one-loop corrections by MIA.

1. The one-loop contributions from $\tilde{B}(\lambda_{\tilde{X}})-\tilde{L}_j^L-\tilde{L}_i^R$.

$$C_2^1(\tilde{L}_j^L, \tilde{L}_i^R, \tilde{B}) = \frac{-1}{2m_{l_j} \Lambda^3} \Delta_{ij}^{LR} g_1^2 \sqrt{x_1} [I_1(x_{\tilde{L}_j^L}, x_1) + I_1(x_{\tilde{L}_i^R}, x_1) - 2I_2(x_{\tilde{L}_j^L}, x_1) - I_2(x_{\tilde{L}_i^R}, x_1)], \quad (15)$$

$$C_2^1(\tilde{L}_j^L, \tilde{L}_i^R, \lambda_{\tilde{X}}) = \frac{-1}{2m_{l_j} \Lambda^3} \Delta_{ij}^{LR} (g_{YX}^2 + \frac{1}{2} g_{YX} g_X) \sqrt{x_{\lambda_{\tilde{X}}}} [I_1(x_{\tilde{L}_j^L}, x_{\lambda_{\tilde{X}}}) + I_1(x_{\tilde{L}_i^R}, x_{\lambda_{\tilde{X}}}) - 2I_2(x_{\tilde{L}_j^L}, x_{\lambda_{\tilde{X}}}) - I_2(x_{\tilde{L}_i^R}, x_{\lambda_{\tilde{X}}})], \quad (16)$$

here, m is the particle mass, with $x = \frac{m^2}{\Lambda^2}$. The functions $I_1(x, y)$ and $I_2(x, y)$ are

$$I_1(x, y) = \frac{1}{32\pi^2} \left\{ \frac{1}{x(x-y)} - \frac{2+2\log x}{(x-y)^2} + \frac{2x \log x - 2y \log y}{(x-y)^3} \right\}, \quad (17)$$

$$I_2(x, y) = \frac{1}{96\pi^2} \left\{ \frac{2}{x(x-y)} - \frac{9+6\log x}{(x-y)^2} + \frac{6x+12x \log x}{(x-y)^3} - \frac{6x^2 \log x - 6y^2 \log y}{(x-y)^4} \right\}. \quad (18)$$

2. The one-loop contributions from $\tilde{B}(\lambda_{\tilde{X}})-\tilde{H}^0-\tilde{L}_j^R-\tilde{L}_i^R$.

$$C_2^2(\tilde{L}_j^R, \tilde{L}_i^R, \tilde{B}, \tilde{H}^0) = \frac{1}{2\Lambda^4} g_1^2 \tan \beta \sqrt{x_1 x_{\mu'_H}} \Delta_{ij}^{RR} [2I_4(x_{\tilde{L}_i^R}, x_1, x_{\mu'_H}) + 3I_3(x_{\tilde{L}_j^R}, x_1, x_{\mu'_H})], \quad (19)$$

$$C_2^2(\tilde{L}_j^R, \tilde{L}_i^R, \lambda_{\tilde{X}}, \tilde{H}^0) = \frac{1}{2\Lambda^4} \frac{1}{2} (2g_{YX} + g_X) (g_{YX} + g_X) \tan \beta \sqrt{x_{\lambda_{\tilde{X}}} x_{\mu'_H}} \Delta_{ij}^{RR} \times [2I_4(x_{\tilde{L}_i^R}, x_{\lambda_{\tilde{X}}}, x_{\mu'_H}) + 3I_3(x_{\tilde{L}_j^R}, x_{\lambda_{\tilde{X}}}, x_{\mu'_H})], \quad (20)$$

here $\mu'_H = \frac{\lambda_H v_S}{\sqrt{2}} + \mu$ and $x_{\mu'_H} = \frac{\mu'^2_H}{\Lambda^2}$. The specific forms of $I_3(x, y, z)$ and $I_4(x, y, z)$ are

$$\begin{aligned}
 I_3(x, y, z) = & \frac{1}{32\pi^2} \left\{ \frac{6x + 12x \log x}{(x-y)(x-z)^3} \right. \\
 & + \frac{6x + 12x \log x}{(x-y)^2(x-z)^2} + \frac{6x + 12x \log x}{(x-y)^3(x-z)} \\
 & - \frac{9 + 6 \log x}{(x-y)(x-z)^2} - \frac{9 + 6 \log x}{(x-y)^2(x-z)} \\
 & + \frac{2}{x(x-y)(x-z)} \\
 & + \frac{6x^2 \log x}{(x-y)(x-z)^4} + \frac{6x^2 \log x}{(x-y)^4(x-z)} \\
 & - \frac{6x^2 \log x}{(x-y)^2(x-z)^3} \\
 & - \frac{6x^2 \log x}{(x-y)^3(x-z)^2} + \frac{6y^2 \log y}{(x-y)^4(y-z)} \\
 & \left. - \frac{6z^2 \log z}{(y-z)(x-z)^4} \right\}, \tag{21}
 \end{aligned}$$

$$\begin{aligned}
 I_4(x, y, z) = & \frac{1}{32\pi^2} \left\{ - \frac{2 + 2 \log x}{(x-y)(x-z)^2} \right. \\
 & - \frac{2 + 2 \log x}{(x-y)^2(x-z)} + \frac{1}{x(x-y)(x-z)} \\
 & + \frac{2x \log x}{(x-y)(x-z)^3} + \frac{2x \log x}{(x-y)^2(x-z)^2} \\
 & + \frac{2x \log x}{(x-y)^3(x-z)} \\
 & \left. - \frac{2y \log y}{(x-y)^3(y-z)} + \frac{2z \log z}{(x-z)^3(y-z)} \right\}. \tag{22}
 \end{aligned}$$

3. The one-loop contributions from $\tilde{B}(\lambda_{\tilde{X}}) - \tilde{H}^0 - \tilde{L}_j^L - \tilde{L}_i^L$.

$$\begin{aligned}
 C_2^3(\tilde{L}_j^L, \tilde{L}_i^L, \tilde{H}^0, \tilde{B}) & \\
 = & \frac{-m_i}{4m_{l_j} \Lambda^4} g_1^2 \tan \beta \sqrt{x_1 x_{\mu'_H}} \Delta_{ij}^{LL} [2I_4(x_{\tilde{L}_i^L}, x_1, x_{\mu'_H}) \\
 & + 3I_3(x_{\tilde{L}_j^L}, x_1, x_{\mu'_H})], \tag{23}
 \end{aligned}$$

$$\begin{aligned}
 C_2^3(\tilde{L}_j^L, \tilde{L}_i^L, \tilde{H}^0, \lambda_{\tilde{X}}) & \\
 = & \frac{-m_i}{4m_{l_j} \Lambda^4} g_{YX}(g_{YX} + g_X) \tan \beta \sqrt{x_{\lambda_{\tilde{X}}} x_{\mu'_H}} \Delta_{ij}^{LL} \\
 & \times [2I_4(x_{\tilde{L}_i^L}, x_{\lambda_{\tilde{X}}}, x_{\mu'_H}) + 3I_3(x_{\tilde{L}_j^L}, x_{\lambda_{\tilde{X}}}, x_{\mu'_H})]. \tag{24}
 \end{aligned}$$

4. The one-loop contributions from $\tilde{W}^0 - \tilde{H}^0 - \tilde{L}_j^L - \tilde{L}_i^L$.

$$\begin{aligned}
 C_2^4(\tilde{L}_j^L, \tilde{L}_i^L, \tilde{H}^0, \tilde{W}^0) & \\
 = & \frac{m_i}{4m_{l_j} \Lambda^4} g_2^2 \tan \beta \sqrt{x_2 x_{\mu'_H}} \Delta_{ij}^{LL} \\
 & \times [2I_4(x_{\tilde{L}_i^L}, x_2, x_{\mu'_H}) + 3I_3(x_{\tilde{L}_j^L}, x_2, x_{\mu'_H})]. \tag{25}
 \end{aligned}$$

5. The one-loop contributions from $\tilde{B} - \lambda_{\tilde{X}} - \tilde{L}_j^L - \tilde{L}_i^R$.

$$\begin{aligned}
 C_2^5(\tilde{L}_j^L, \tilde{L}_i^R, \tilde{B}, \lambda_{\tilde{X}}) & \\
 = & \frac{-1}{2m_{l_j} \Lambda^3} \Delta_{ij}^{LR} g_{1g_{YX}} \sqrt{x_{BB'} x_1 x_{\lambda_{\tilde{X}}}} [I_4(x_{\tilde{L}_j^L}, x_1, x_{\lambda_{\tilde{X}}}) \\
 & + I_4(x_{\tilde{L}_i^R}, x_1, x_{\lambda_{\tilde{X}}}) + I_5(x_{\tilde{L}_j^L}, x_1, x_{\lambda_{\tilde{X}}}) + 2I_5(x_{\tilde{L}_i^R}, x_1, x_{\lambda_{\tilde{X}}})] \\
 & + \frac{1}{2m_{l_j} \Lambda^3} \Delta_{ij}^{LR} g_{1g_{YX}} \sqrt{x_{BB'}} [I_6(x_{\tilde{L}_j^L}, x_1, x_{\lambda_{\tilde{X}}}) \\
 & + I_6(x_{\tilde{L}_i^R}, x_1, x_{\lambda_{\tilde{X}}}) + I_7(x_{\tilde{L}_j^L}, x_1, x_{\lambda_{\tilde{X}}}) + 2I_7(x_{\tilde{L}_i^R}, x_1, x_{\lambda_{\tilde{X}}})]. \tag{26}
 \end{aligned}$$

We show the one-loop functions $I_5(x, y, z)$ and $I_6(x, y, z)$ in the following form

$$\begin{aligned}
 I_5(x, y, z) = & \frac{-1}{32\pi^2} \left\{ \frac{3 + 2 \log x}{(x-y)(x-z)} \right. \\
 & - \frac{2x + 4x \log x}{(x-y)(x-z)^2} - \frac{2x + 4x \log x}{(x-y)^2(x-z)} \\
 & + \frac{2x^2 \log x}{(x-y)(x-z)^3} + \frac{2x^2 \log x}{(x-y)^2(x-z)^2} + \frac{2x^2 \log x}{(x-y)^3(x-z)} \\
 & \left. - \frac{2y^2 \log y}{(x-y)^3(y-z)} + \frac{2z^2 \log z}{(x-z)^3(y-z)} \right\}, \tag{27}
 \end{aligned}$$

$$\begin{aligned}
 I_6(x, y, z) = & \frac{1}{96\pi^2} \left\{ \frac{6x^2(3x^2 + y^2 + z^2 + yz - 3xy - 3xz)(1 + 3 \log x)}{(x-y)^3(x-z)^3} \right. \\
 & - \frac{(6x^2 - 3xy - 3xz)(5 + 6 \log x)}{(x-y)^2(x-z)^2} + \frac{6y^3 \log y - 6x^3 \log x}{(x-y)^4(y-z)} \\
 & \left. + \frac{11 + 6 \log x}{(x-y)(x-z)} + \frac{6x^3 \log x - 6z^3 \log z}{(x-z)^4(y-z)} \right\}. \tag{28}
 \end{aligned}$$

6. The one-loop contributions from chargino and left-handed CP-even(odd) sneutrino.

$$\begin{aligned}
 C_2^6(\tilde{\nu}_{L_j}^I, \tilde{\nu}_{L_i}^I, \tilde{H}^\pm, \tilde{W}^\pm) & \\
 = & \frac{1}{2\Lambda^4} g_2^2 \Delta_{ij}^{LL} \tan \beta \{ (\sqrt{x_2 x_{\mu'_H}} + x_{\mu'_H}) I_8(x_{\mu'_H}, x_2, x_{\tilde{\nu}_{L_i}^I}) \\
 & + (\sqrt{x_2 x_{\mu'_H}} + x_2) I_8(x_2, x_{\mu'_H}, x_{\tilde{\nu}_{L_j}^I}) \\
 & + \sqrt{x_2 x_{\mu'_H}} I_9(x_2, x_{\mu'_H}, x_{\tilde{\nu}_{L_i}^I}) - I_{10}(x_2, x_{\mu'_H}, x_{\tilde{\nu}_{L_j}^I}) \}, \tag{29}
 \end{aligned}$$

$$\begin{aligned}
 C_2^6(\tilde{\nu}_{L_j}^R, \tilde{\nu}_{L_i}^R, \tilde{H}^\pm, \tilde{W}^\pm) & \\
 = & \frac{1}{2\Lambda^4} g_2^2 \Delta_{ij}^{LL} \tan \beta \{ (\sqrt{x_2 x_{\mu'_H}} + x_{\mu'_H}) I_8(x_{\mu'_H}, x_2, x_{\tilde{\nu}_{L_i}^R}) \\
 & + (\sqrt{x_2 x_{\mu'_H}} + x_2) I_8(x_2, x_{\mu'_H}, x_{\tilde{\nu}_{L_j}^R}) \\
 & + \sqrt{x_2 x_{\mu'_H}} I_9(x_2, x_{\mu'_H}, x_{\tilde{\nu}_{L_i}^R}) - I_{10}(x_2, x_{\mu'_H}, x_{\tilde{\nu}_{L_j}^R}) \}. \tag{30}
 \end{aligned}$$

The one-loop functions $I_7(x, y, z)$, $I_8(x, y, z)$ and $I_9(x, y, z)$ read as

$$\begin{aligned}
 I_7(x, y, z) = & \frac{-1}{32\pi^2} \left[\frac{8x \log x - 4x}{(x-y)(x-z)^3} \right. \\
 & \left. - \frac{2x + 4x \log x}{(x-y)^2(x-z)^2} + \frac{3 + 2 \log x}{(x-y)(x-z)^2} \right]
 \end{aligned}$$

$$\begin{aligned}
 & + \frac{2z + 4z \log z}{(x - z)^3(y - z)} + \frac{4x^2 \log x}{(x - y)^2(x - z)^3} \\
 & - \frac{2x^2 \log x}{(x - y)^3(x - z)^2} \\
 & + \frac{2z^3 \log z}{(x - z)^3(y - z)^2} - \frac{2y^2 \log y}{(x - y)^3(y - z)^2} \\
 & + \left. \frac{6x^2 \log x}{(x - y)(x - z)^4} + \frac{6z^2 \log z}{(x - z)^4(y - z)} \right], \tag{31}
 \end{aligned}$$

$$\begin{aligned}
 I_8(x, y, z) = & \frac{-1}{16\pi^2} \left[\frac{x + 2x \log x}{(x - y)^2(x - z)^2} \right. \\
 & + \frac{y + 2y \log y}{(x - y)^2(y - z)^2} + \frac{z + 2z \log z}{(x - z)^2(y - z)^2} \\
 & - \frac{2x^2 \log x}{(x - y)^2(x - z)^3} - \frac{2x^2 \log x}{(x - y)^3(x - z)^2} \\
 & - \frac{2y^2 \log y}{(x - y)^2(y - z)^3} \\
 & + \frac{2y^2 \log y}{(x - y)^3(y - z)^2} + \frac{2z^2 \log z}{(x - z)^2(y - z)^3} \\
 & \left. + \frac{2z^2 \log z}{(x - z)^3(y - z)^2} \right], \tag{32}
 \end{aligned}$$

$$\begin{aligned}
 I_9(x, y, z) = & \frac{1}{96\pi^2} \left[\frac{x^2 + 3x^2 \log x}{(x - y)(x - z)^2} \right. \\
 & + \frac{3z^2 \log z - z^2}{(x - z)^2(y - z)} - \frac{2x^3 \log x}{(x - y)(x - z)^3} \\
 & - \frac{2z^3 \log z}{(x - z)^3(y - z)} - \frac{x^3 \log x}{(x - y)^2(x - z)^2} \\
 & \left. + \frac{y^3 \log y}{(x - y)^2(y - z)^2} - \frac{z^3 \log z}{(x - z)^2(y - z)^2} \right]. \tag{33}
 \end{aligned}$$

From the above formulas, we can find that C_2^f ($f = 1 \dots 6$) are mostly affected by $\tan \beta$ and Δ_{ij}^{AB} ($A, B = L, R$) and there is a positive correlation. Δ_{ij}^{AB} have the lepton flavor violating sources. It provides a reference for our subsequent work. Finally, we get the final Wilson coefficient and decay width of $l_j \rightarrow l_i \gamma$,

$$C_2 = \sum_i^{i=1 \dots 6} C_2^i, \Gamma(l_j \rightarrow l_i \gamma) = \frac{e^2}{8\pi} m_{l_j}^5 |C_2|^2. \tag{34}$$

The branching ratio of $l_j \rightarrow l_i \gamma$ is

$$Br(l_j \rightarrow l_i \gamma) = \Gamma(l_j \rightarrow l_i \gamma) / \Gamma_{l_j}. \tag{35}$$

3.2 Degenerate result

In order to more intuitively analyze the factors affecting lepton flavor violating processes $l_j \rightarrow l_i \gamma$, we suppose that all the masses of the superparticles are almost degenerate. In other words, we give the one-loop results (chargino-sneutrino, neutralino-slepton) in the extreme case, where the masses for superparticles ($M_1, M_2, \mu'_H, m_{\tilde{L}_L}, m_{\tilde{L}_R}, M_{\lambda_{\tilde{X}}}, M_{BB'}$) are equal to M_{SUSY} [20]:

$$\begin{aligned}
 M_1 = |M_2| = \mu'_H = m_{\tilde{L}_L} = m_{\tilde{L}_R} = M_{\lambda_{\tilde{X}}} \\
 = |M_{BB'}| = M_{SUSY}.
 \end{aligned}$$

The functions I_i ($i = 1 \dots 9$) and Δ_{ij}^{AB} ($A, B = L, R$) are much simplified as

$$\begin{aligned}
 I_1(1, 1) = \frac{-1}{96\pi^2}, \quad I_2(1, 1) = \frac{-1}{192\pi^2}, \quad I_3(1, 1, 1) = \frac{-1}{480\pi^2}, \\
 I_4(1, 1, 1) = \frac{1}{192\pi^2}, \quad I_5(1, 1, 1) = \frac{1}{192\pi^2}, \quad I_6(1, 1, 1) = \frac{-1}{320\pi^2}, \\
 I_7(1, 1, 1) = \frac{-1}{480\pi^2}, \quad I_8(1, 1, 1) = \frac{-1}{480\pi^2}, \\
 I_9(1, 1, 1) = \frac{1}{384\pi^2}, \tag{36}
 \end{aligned}$$

$$\begin{aligned}
 \Delta_{ij}^{LR} = m_{l_j} m_{\tilde{L}_L} \delta_{ij}^{LR}, \quad \Delta_{ij}^{LL} = m_{\tilde{L}_L}^2 \delta_{ij}^{LL}, \\
 \Delta_{ij}^{RR} = m_{\tilde{L}_R}^2 \delta_{ij}^{RR}. \tag{37}
 \end{aligned}$$

Then, we obtain the much simplified one-loop results of C_2

$$\begin{aligned}
 C_2 = & \frac{(2g_1^2 \text{sign}[M_1 \mu'_H] + (2g_{YX}^2 + 3g_{YX}g_X + g_X^2) \text{sign}[M_{\lambda_{\tilde{X}}} \mu'_H]) \tan \beta \delta_{ij}^{RR}}{960\pi^2 M_{SUSY}^2} \\
 & + \frac{(-g_1^2 \text{sign}[M_1 \mu'_H] - (g_{YX}^2 + g_{YX}g_X) \text{sign}[M_{\lambda_{\tilde{X}}} \mu'_H] + g_2^2 \text{sign}[M_2 \mu'_H]) m_{l_i} \tan \beta \delta_{ij}^{LL}}{960\pi^2 M_{SUSY}^2 m_{l_j}} \\
 & + \frac{(-4g_2^2 \text{sign}[M_2^2] - 4g_2^2 \text{sign}[\mu_H^2] - 12g_2^2 \text{sign}[\mu'_H M_2] + 5g_2^2) \tan \beta \delta_{ij}^{LL}}{3840\pi^2 M_{SUSY}^2} \\
 & + \frac{1}{1920\pi^2 M_{SUSY}^2} \times \{(5g_1^2 \text{sign}[M_1] + 5(g_{YX}^2 + \frac{1}{2}g_{YX}g_X) \text{sign}[M_{\lambda_{\tilde{X}}}] \\
 & - 4g_1g_{YX} \text{sign}[M_{BB'} M_1 M_{\lambda_{\tilde{X}}}] + g_1g_{YX} \text{sign}[M_{BB'}]) \delta_{ij}^{LR}\}. \tag{38}
 \end{aligned}$$

In the above formula, after simple approximation, we can find that in the formula of the second line, due to the existence of $\frac{m_{l_i}}{m_{l_j}}$, the result is 2–3 orders of magnitude smaller than other terms. Therefore, we will not consider the term with $\frac{m_{l_i}}{m_{l_j}}$ here. It can be found that $\text{sign}[M_1], \text{sign}[M_2], \text{sign}[M_{\lambda_{\tilde{\chi}}}], \text{sign}[\mu'_H]$ and $\text{sign}[M_{BB'}]$ have a certain impact on the correction of C_2 . According to $1 > g_X > g_{YX} > 0$, we assume $\text{sign}[M_1] = \text{sign}[M_{\lambda_{\tilde{\chi}}}] = \text{sign}[\mu'_H] = 1$ and $\text{sign}[M_2] = \text{sign}[M_{BB'}] = -1$, and get the larger value of C_2

$$C_2 = \frac{(5g_1^2 + 5(g_{YX}^2 + \frac{1}{2}g_{YX}g_X) + 3g_1g_{YX})\delta_{ij}^{LR}}{1920\pi^2 M_{SUSY}^2} + \frac{3g_2^2 \tan \beta \delta_{ij}^{LL}}{1280\pi^2 M_{SUSY}^2} + \frac{(2g_1^2 + (2g_{YX}^2 + 3g_{YX}g_X + g_X^2)) \tan \beta \delta_{ij}^{RR}}{960\pi^2 M_{SUSY}^2}. \tag{39}$$

Due to the different orders of magnitude of branching ratios, we set $\tan \beta = 9$, $M_{SUSY} = 1000$ GeV and discuss in two cases:

1. $\mu \rightarrow e\gamma$

We take $g_{YX}, g_X, \delta_{ij}^{LR}, \delta_{ij}^{LL}$ and δ_{ij}^{RR} as variables to study the effect on $Br(\mu \rightarrow e\gamma)$. In Fig. 2, it can be found that both δ_{ij}^{LR} and δ_{ij}^{RR} have great influence on $Br(\mu \rightarrow e\gamma)$ and they are all increasing trend. The larger the values of δ_{ij}^{LR} and δ_{ij}^{RR} , the easier it is to approach the upper limit of the experiment.

Similar to the above, in Fig. 3, with the increase of δ_{ij}^{LL} , the value of $Br(\mu \rightarrow e\gamma)$ gradually increases, and when g_X increases, $Br(\mu \rightarrow e\gamma)$ also increases. When $\delta_{ij}^{LL} = 9 \times 10^{-4}$ and $g_X = 0.65$, $Br(\mu \rightarrow e\gamma)$ reaches the experimental upper limit. But in numerical terms, the effect of δ_{ij}^{LL} is greater than g_X .

2. $\tau \rightarrow \mu(e)\gamma$

Since the numerical results of $Br(\tau \rightarrow \mu\gamma)$ and $Br(\tau \rightarrow e\gamma)$ are close and have similar characteristic, we take $\tau \rightarrow \mu\gamma$ as an example. In Fig. 4, when the values of δ_{ij}^{RR} and g_X enlarger, the value of $Br(\tau \rightarrow \mu\gamma)$ also increases, which can well reach the experimental measured value.

In Fig. 5, we analyze δ_{ij}^{LL} and g_{YX} on the $Br(\tau \rightarrow \mu\gamma)$. The value of $Br(\tau \rightarrow \mu\gamma)$ also increases with the increasing δ_{ij}^{LL} and g_{YX} , but the effect from g_{YX} is greater than δ_{ij}^{LL} . So the correction of g_{YX} to $Br(\tau \rightarrow \mu\gamma)$ is greater than that of δ_{ij}^{LL} .

All in all, we can find that $g_{YX}, g_X, \delta_{ij}^{LR}, \delta_{ij}^{LL}$ and δ_{ij}^{RR} all have direct impact on the correction to $Br(\mu \rightarrow e\gamma), Br(\tau \rightarrow \mu\gamma)$ and $Br(\tau \rightarrow e\gamma)$.

3.3 Muon anomalous magnetic moment

The one-loop corrections to muon anomalous magnetic moment are obtained with MIA. Here, we show the one-loop contributions from chargino and CP-even(odd) sneutrino as [20]

$$a_\mu(\tilde{\nu}_L^R, \tilde{H}^\pm, \tilde{W}^\pm) = \frac{g_2^2}{2} x_\mu \sqrt{x_2 x_{\mu'_H}} \tan \beta [2\mathcal{I}(x_{\mu'_H}, x_{\tilde{\nu}_L^R}, x_2) - \mathcal{J}(x_2, x_{\mu'_H}, x_{\tilde{\nu}_L^R}) + 2\mathcal{I}(x_2, x_{\tilde{\nu}_L^R}, x_{\mu'_H}) - \mathcal{J}(x_{\mu'_H}, x_2, x_{\tilde{\nu}_L^R})], \tag{40}$$

$$a_\mu(\tilde{\nu}_L^I, \tilde{H}^\pm, \tilde{W}^\pm) = \frac{g_2^2}{2} x_\mu \sqrt{x_2 x_{\mu'_H}} \tan \beta [2\mathcal{I}(x_{\mu'_H}, x_{\tilde{\nu}_L^I}, x_2) - \mathcal{J}(x_2, x_{\mu'_H}, x_{\tilde{\nu}_L^I}) + 2\mathcal{I}(x_2, x_{\tilde{\nu}_L^I}, x_{\mu'_H}) - \mathcal{J}(x_{\mu'_H}, x_2, x_{\tilde{\nu}_L^I})]. \tag{41}$$

The concrete forms of the one-loop functions $\mathcal{I}(x, y, z)$ and $\mathcal{J}(x, y, z)$ are

$$\mathcal{J}(x, y, z) = \frac{1}{16\pi^2} \left[\frac{x(x^2 + xz - 2yz) \log x}{(x - y)^2(x - z)^3} - \frac{y^2 \log y}{(x - y)^2(y - z)^2} + \frac{z[x(z - 2y) + z^2] \log z}{(z - x)^3(y - z)^2} - \frac{x(y - 2z) + yz}{(x - y)(x - z)^2(y - z)} \right]. \tag{42}$$

$$\mathcal{I}(x, y, z) = \frac{1}{16\pi^2} \left[\frac{1}{(x - z)(z - y)} + \frac{(z^2 - xy) \log z}{(x - z)^2(y - z)^2} - \frac{x \log x}{(x - y)(x - z)^2} + \frac{y \log y}{(x - y)(y - z)^2} \right]. \tag{43}$$

The other one-loop contributions are obtained from $\tilde{B}(\lambda_{\tilde{\chi}}) - \tilde{L}_L - \tilde{L}_R, \tilde{B}(\lambda_{\tilde{\chi}}) - \tilde{H}^0 - \tilde{L}_R, \tilde{B}(\tilde{W}^0, \lambda_{\tilde{\chi}}) - \tilde{H}^0 - \tilde{L}_L$ and $\tilde{B} - \lambda_{\tilde{\chi}} - \tilde{L}_R - \tilde{L}_L$. To save space in the text, we do not show their concrete forms here, which can be found in Ref. [20]. In our previous work [20], the one-loop contributions of muon anomalous magnetic moment in the degenerate form are get with the supposition $M_1 = M_2 = \mu'_H = m_{\tilde{L}_L} = m_{\tilde{L}_R} = |M_{\lambda_{\tilde{\chi}}}| = |M_{BB'}| = M_{SUSY}$

$$a_\mu^{1L} \simeq \frac{1}{192\pi^2} \frac{m_\mu^2}{M_{SUSY}^2} \tan \beta (5g_2^2 + g_1^2) + \frac{1}{960\pi^2} \frac{m_\mu^2}{M_{SUSY}^2} \tan \beta \left[5(g_{YX}^2 - g_{YX}g_X - g_X^2) \text{sign}[M_{\lambda_{\tilde{\chi}}}] + g_1(4g_{YX} + g_X) \text{sign}[M_{BB'}] (1 - 4\text{sign}[M_{\lambda_{\tilde{\chi}}}] \right]. \tag{44}$$

4 Numerical results

In this section, we study the numerical results and consider the constraints from lepton flavor violating processes $l_j \rightarrow l_i\gamma$. In addition, we have considered the following conditions: 1. the lightest CP-even Higgs mass $m_{h^0} = 125.1$ GeV [34, 35]. 2. The latest experimental results of the mass of the heavy

Fig. 2 Under the condition that $g_{YX} = 0.2$, $g_X = 0.3$ and $\delta_{ij}^{LL} = 1 \times 10^{-3}$, the effect of δ_{ij}^{LR} and δ_{ij}^{RR} on $Br(\mu \rightarrow e\gamma)$. The x-axis representing the range of δ_{ij}^{LR} is from 1×10^{-5} to 1×10^{-2} , and the y-axis represents $1 \times 10^{-5} < \delta_{ij}^{RR} < 1 \times 10^{-3}$. The rightmost icon is the color corresponding to the value of $Br(\mu \rightarrow e\gamma)$

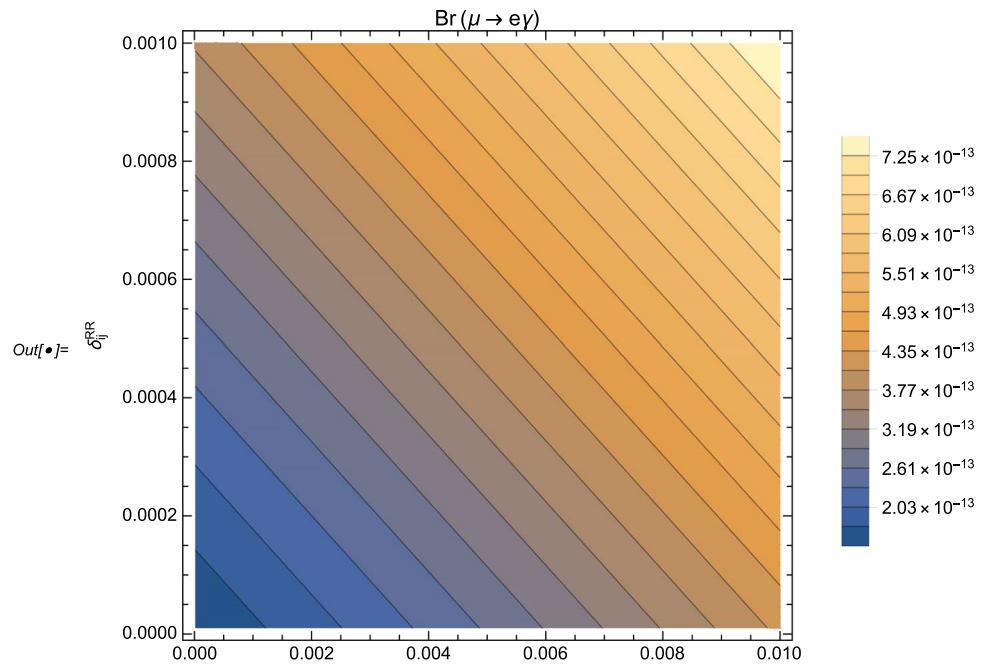
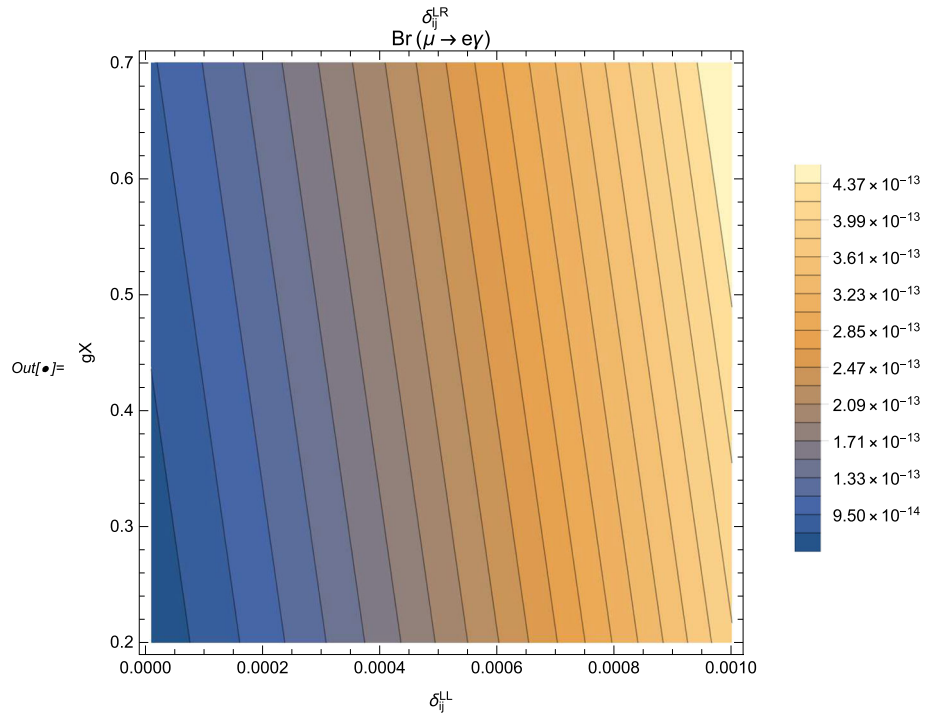


Fig. 3 Under the condition that $g_{YX} = 0.2$, $\delta_{ij}^{RR} = 1 \times 10^{-6}$ and $\delta_{ij}^{LR} = 1 \times 10^{-2}$, δ_{ij}^{LL} versus g_X about $Br(\mu \rightarrow e\gamma)$. The abscissa is $1 \times 10^{-5} < \delta_{ij}^{LL} < 1 \times 10^{-3}$ and the ordinate represents $0.2 < g_X < 0.7$. The icon on the right shows the value of $Br(\mu \rightarrow e\gamma)$



vector boson Z' is $M_{Z'} > 5.1$ TeV [36]. 3. The limits for the masses of other particles beyond SM. 4. The bound on the ratio between $M_{Z'}$ and its gauge coupling g_X is $M_{Z'}/g_X \geq 6$ TeV at 99% CL [37,38]. 5. The constraint from LHC data, $\tan \beta_\eta < 1.5$ [39]. 6. The scalar lepton masses larger than 700 GeV and chargino masses larger than 1100 GeV [40].

Considering the above constraints in the front paragraph, we use the following parameters

$$M_S = 2.7 \text{ TeV}, T_\kappa = 1.6 \text{ TeV}, M_1 = 1.2 \text{ TeV}, \\ M_2 = M_{BL} = 1 \text{ TeV}, g_{YX} = 0.2,$$

$$\xi = 17 \text{ TeV}, Y_{X11} = Y_{X22} = Y_{X33} = 1, g_X = 0.3, \\ \kappa = 1, \lambda_C = -0.08, v_S = 4.3 \text{ TeV}, \\ M_{BB'} = 0.4 \text{ TeV}, T_{\lambda_H} = 0.3 \text{ TeV}, M_{\tilde{L}11}^2 = M_{\tilde{L}22}^2 \\ = M_{\tilde{L}33}^2 = M_{\tilde{L}}^2 = 0.5 \text{ TeV}^2, l_W = 4 \text{ TeV}^2, \\ \lambda_H = 0.1, T_{e11} = T_{e22} = T_{e33} = 5 \text{ TeV}, \tan \beta_\eta = 0.8, \\ B_\mu = B_S = 1 \text{ TeV}^2, \mu = 0.5 \text{ TeV}, \\ T_{\lambda_C} = -0.1 \text{ TeV}, M_{\tilde{E}11}^2 = M_{\tilde{E}22}^2 \\ = M_{\tilde{E}33}^2 = M_{\tilde{E}}^2 = 3.6 \text{ TeV}^2. \tag{45}$$

Fig. 4 Under the condition that $\delta_{ij}^{LR} = 0.1$, $g_{YX} = 0.2$ and $\delta_{ij}^{LL} = 0.1$, the effect of δ_{ij}^{RR} and g_X on $Br(\tau \rightarrow \mu\gamma)$. The x-axis representing the range of δ_{ij}^{RR} is from 10^{-5} to 1, and the y-axis represents $0.2 < g_X < 0.7$. The rightmost icon is the color corresponding to the value of $Br(\tau \rightarrow \mu\gamma)$

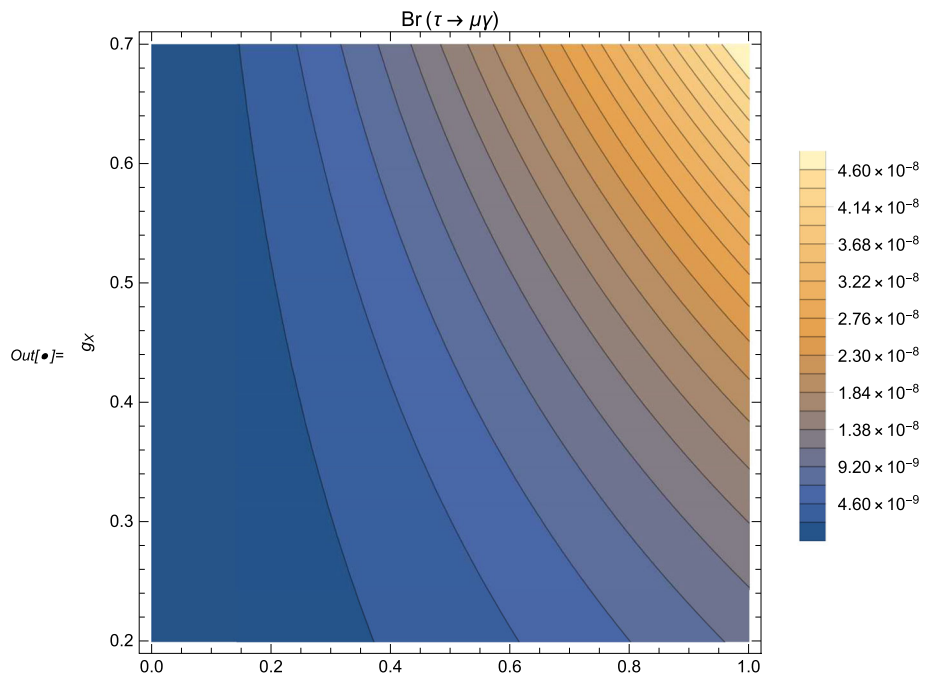
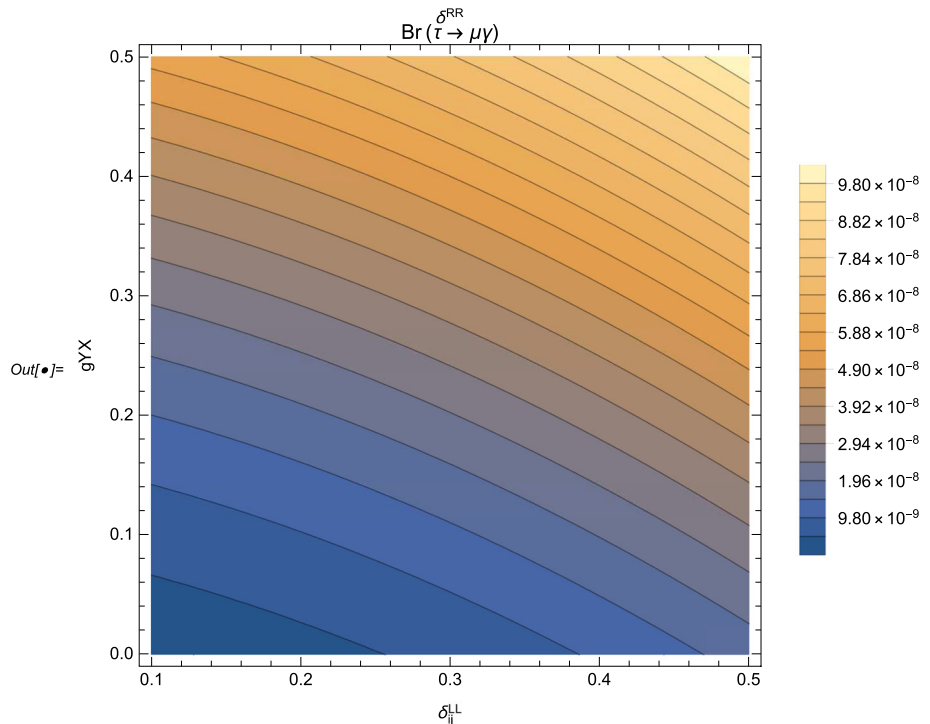


Fig. 5 Under the condition that $\delta_{ij}^{RR} = 0.2$, $g_X = 0.3$ and $\delta_{ij}^{LR} = 0.5$, δ_{ij}^{LL} versus g_{YX} about $Br(\tau \rightarrow \mu\gamma)$. The abscissa is $1 \times 10^{-5} < \delta_{ij}^{LL} < 0.5$ and the ordinate represents $0.1 < g_{YX} < 0.5$. The icon on the right shows the value of $Br(\tau \rightarrow \mu\gamma)$



To simplify the numerical research, we use the relations for the parameters and they vary in the following numerical analysis

$$\begin{aligned}
 M_{L12}^2 &= M_{L21}^2, M_{L13}^2 = M_{L31}^2, M_{L32}^2 = M_{L23}^2, \\
 M_{E12}^2 &= M_{E21}^2, M_{E13}^2 = M_{E31}^2, M_{E23}^2 = M_{E32}^2, \\
 T_{e12} &= T_{e21}, T_{e13} = T_{e31}, T_{e23} = T_{e32}, \tan \beta.
 \end{aligned}
 \tag{46}$$

Without special statement, the non-diagonal elements of the parameters are supposed as zero.

4.1 Muon anomalous magnetic moment

In this subsection, we study the one-loop $g - 2$ in $U(1)_X$ SSM model by MIA and expect to get some inspiration about using MIA to find LFV. The new experiment data of muon $g - 2$ is reported by the workers at Fermilab National Accelerator Laboratory (FNAL) [41–44]. Combined with the previous Brookhaven National Laboratory (BNL) E821 result [45], we get the new averaged experiment value of muon anomaly is $a_\mu^{\text{exp}} = 116592061(41) \times 10^{-11}$ (0.35 ppm). The departure

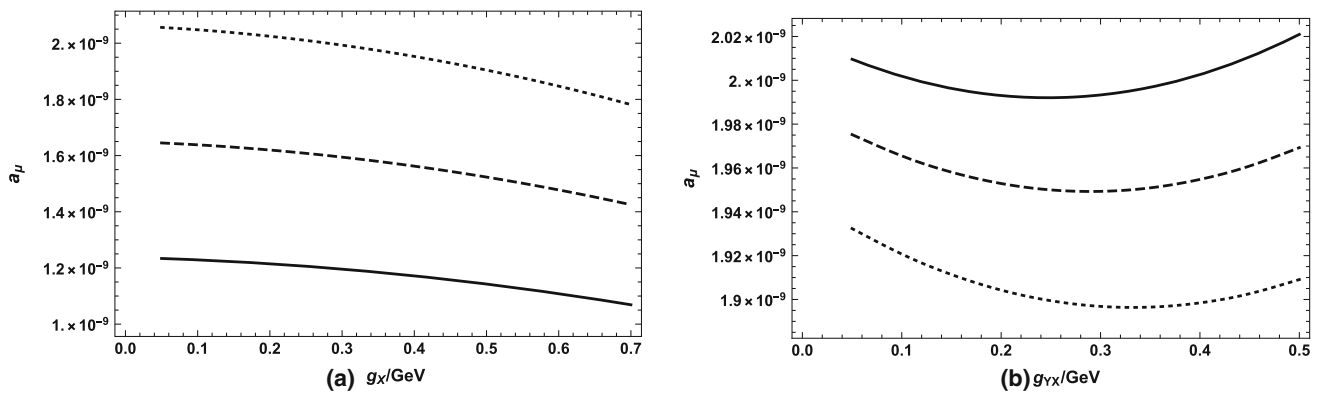


Fig. 6 a_μ versus g_X (a) and g_{YX} (b). The dotted line, dashed line and solid line in a correspond to $\tan \beta$ equal to 50, 40 and 30 respectively. In b, the solid (dashed, dotted) line corresponds to the results with $g_X = 0.3$ (0.4, 0.5)

from the SM prediction is $\Delta a_\mu = a_\mu^{\text{exp}} - a_\mu^{\text{SM}} = 251(59) \times 10^{-11}$, which is about 4.2σ . We set the particle masses as: $M_1 = 800$ GeV, $\mu = 350$ GeV, $m_{\tilde{\nu}_L^R} = 150$ GeV, $m_{\tilde{\nu}_L^I} = 140$ GeV, $m_{\tilde{L}_L} = 800$ GeV, $m_{\tilde{L}_R} = 850$ GeV and $m_{\lambda_{\tilde{X}}} = 450$ GeV to get Fig. 6. When $g_{YX} = 0.2$ in Fig. 6a, we can see that from bottom to top are solid line ($\tan \beta = 30$), dashed line ($\tan \beta = 40$) and dotted line ($\tan \beta = 50$) and the overall trend of the three lines is downward. That is to say, $\tan \beta$ is a sensitive parameter and larger $\tan \beta$ leads to larger a_μ .

We set $\tan \beta = 50$ in Fig. 6b. It is obvious that three lines with the same tendency to decrease and then increase. The dotted line ($g_X = 0.5$) is below the dashed line ($g_X = 0.4$), and the dashed line is below the solid line ($g_X = 0.3$). When g_X increases, a_μ decreases. The influence of g_{YX} on a_μ mainly depends on its own value: when g_{YX} is less than 0.3, g_{YX} increases and a_μ decreases, but when $g_{YX} > 0.3$, the situation is just the opposite. The value of a_μ can reach 2×10^{-9} at most, it can reach about 80% of the departure (Δa_μ), which better meets the experimental limitations. The above conclusion is the same as Eq. (44), so we can find other sensitive parameters more intuitively through formula Eq. (44).

4.2 The processes of $\mu \rightarrow e\gamma$

In order to study the parameters affecting LFV, we need to study some sensitive parameters. To show the numerical results clearly, we draw the relation diagrams and scatter diagrams of $Br(\mu \rightarrow e\gamma)$ with different parameters.

The gray area is current limit on LFV decay $\mu \rightarrow e\gamma$ in Fig. 7. With the parameters $M_{L12}^2 = 0$, $M_{E12}^2 = 0$ and $T_{e12} = 0$, we plot $Br(\mu \rightarrow e\gamma)$ versus $m_{\tilde{\nu}_L}$ in the Fig. 7a. The dashed curve corresponds to $M_{L12}^2 = 500$ GeV² and the solid line corresponds to $M_{L12}^2 = 200$ GeV². On the whole, both lines show a downward trend. $m_{\tilde{\nu}_L}$ and $Br(\mu \rightarrow e\gamma)$ are inversely proportional. The smaller $m_{\tilde{\nu}_L}$ is, the greater the value of $Br(\mu \rightarrow e\gamma)$ is. Separately, the dashed line is larger than the solid line, and the ranges consistent with the experimental

value are 1400 GeV–4000 GeV and 900 GeV–1400 GeV respectively. m_{L12}^2 and $Br(\mu \rightarrow e\gamma)$ are positively correlated. If the value of M_{L12}^2 gets smaller, the value of $m_{\tilde{\nu}_L}$ can be less than 1000 GeV.

We show $Br(\mu \rightarrow e\gamma)$ varying with M_{L12}^2 by the solid curve ($T_{e12} = 100$ GeV) and dashed curve ($T_{e12} = 50$ GeV) in the Fig. 7b. We can see that the overall values meet the limit, and the trend is a subtractive function, and the solid line is greater than the dotted line. So we can conclude that as T_{e12} increases, $Br(\mu \rightarrow e\gamma)$ also increases. When M_{L12}^2 increases, $Br(\mu \rightarrow e\gamma)$ decreases. The numerical results are tiny and at the order of 10^{-19} .

Finally, we analyze the effects of the parameter T_{e12} on branching ratio of $\mu \rightarrow e\gamma$. The numerical results are shown in the Fig. 7c by the dashed curve ($\tan \beta = 9$) and solid curve ($\tan \beta = 20$). The value of the solid line is greater than that of the dashed line, and both show an upward trend. Therefore, The relationship between $\tan \beta$ and $Br(\mu \rightarrow e\gamma)$, T_{e12} and $Br(\mu \rightarrow e\gamma)$ is the similar, and they are all positively correlated.

For more multidimensional analysis of sensitive parameters, we scatter points according to Table 1 (part of $\mu \rightarrow e\gamma$) to get Fig. 8. We set the range of \blacklozenge ($0 < Br(\mu \rightarrow e\gamma) < 1.5 \times 10^{-13}$), \blacktriangle ($1.5 \times 10^{-13} \leq Br(\mu \rightarrow e\gamma) < 3.5 \times 10^{-13}$) and \bullet ($3.5 \times 10^{-13} \leq Br(\mu \rightarrow e\gamma) < 4.2 \times 10^{-13}$) to represent the results in different parameter spaces for the process of $\mu \rightarrow e\gamma$.

The relationship between M_{L12}^2 and $m_{\tilde{L}}$ is shown in Fig. 8a. \blacklozenge are mainly concentrated in the upper left corner, then the outer layer are \blacktriangle and finally \bullet . When M_{L12}^2 is near 0 and $m_{\tilde{L}}$ is near 2500 GeV, $Br(\mu \rightarrow e\gamma)$ gets the minimum value. Figure 8b is plotted in the plane of $m_{\tilde{L}}$ versus $m_{\tilde{\nu}_L}$. We can clearly find that the points are mainly concentrated in the right, and the color gradually deepens from lower left to upper right. The effects of M_{L12}^2 and $m_{\tilde{\nu}_L}$ on $Br(\mu \rightarrow e\gamma)$ are shown in the Fig. 8c. All points are mainly concentrated in the upper left corner and on both sides of axis $M_{L12}^2 = 0$

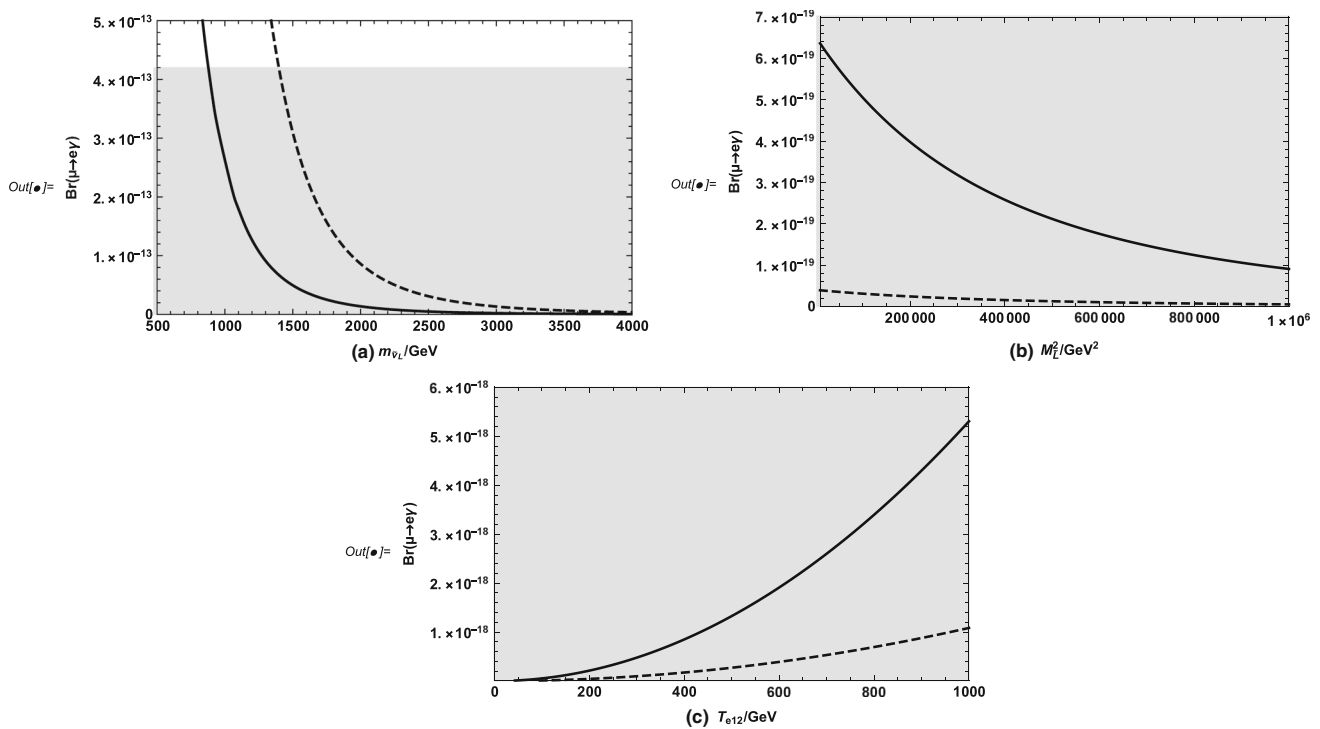


Fig. 7 $Br(\mu \rightarrow e\gamma)$ schematic diagrams affected by different parameters. The gray area is reasonable value range, where $Br(\mu \rightarrow e\gamma)$ is lower than the upper limit. As $T_{e12} = 0$, the dashed and solid lines in **a** correspond to $M_{L12}^2 = 500 \text{ GeV}^2$ and $M_{L12}^2 = 200 \text{ GeV}^2$. The dashed

line and solid line respectively represent $T_{e12} = 50 \text{ GeV}$ and 100 GeV in **b**. We set $M_L^2 = 5 \times 10^5 \text{ TeV}^2$, the dashed line ($\tan \beta = 9$) and solid line ($\tan \beta = 20$) in **c** are generated

and axis $m_{\tilde{\nu}_L} = 3000 \text{ GeV}$. From the inside to the outside, they are \blacklozenge , \blacktriangle and \bullet . When M_{L12}^2 becomes larger and $m_{\tilde{\nu}_L}$ becomes smaller, the value of $Br(\mu \rightarrow e\gamma)$ increases to reach the experimental measurement. Figure 8d shows the effect of $\tan \beta$ and M_{L12}^2 on $Br(\mu \rightarrow e\gamma)$. All points are mainly concentrated near the x-axis, and the value increases from bottom to top.

4.3 The processes of $\tau \rightarrow \mu\gamma$

To study the influence of parameters M_{L23}^2 and M_{E23}^2 on $Br(\tau \rightarrow \mu\gamma)$ in Fig. 9, we suppose the parameters $M_{L12}^2 = 0$, $M_{E12}^2 = 0$ and $T_{e12} = 0$ and plot the solid line ($\tan \beta = 9$) and dashed line ($\tan \beta = 20$). In Fig. 9a, we can see that M_{L23}^2 corresponds to $Br(\tau \rightarrow \mu\gamma)$. We plot M_{E23}^2 varying with $Br(\tau \rightarrow \mu\gamma)$ in the Fig. 9b. Both figures show an upward trend within the experimental limit, and the dashed line is larger than the solid line, so we can draw a conclusion: when M_{L23}^2 or M_{E23}^2 increases, $Br(\tau \rightarrow \mu\gamma)$ also increases. In the whole, the numerical results in Fig. 9 are very tiny.

We scatter points according to the parameters given in Table 1 (part of $\tau \rightarrow \mu\gamma$) to obtain Fig. 10. Where \blacklozenge , \blacktriangle and \bullet represent ($0 < Br(\tau \rightarrow \mu\gamma) < 1.0 \times 10^{-10}$), ($1.0 \times$

$10^{-10} \leq Br(\tau \rightarrow \mu\gamma) < 9.0 \times 10^{-10}$) and ($9.0 \times 10^{-10} \leq Br(\tau \rightarrow \mu\gamma) < 4.4 \times 10^{-8}$) respectively.

M_{L23}^2 corresponds to $m_{\tilde{L}}$ in Fig. 10a. Horizontally, \blacklozenge are mainly concentrated in $0 < M_{L23}^2 < 1500 \text{ GeV}^2$, \blacktriangle are in $1500 \text{ GeV}^2 < M_{L23}^2 < 3200 \text{ GeV}^2$, and \bullet are distributed in $3200 \text{ GeV}^2 < M_{L23}^2 < 5000 \text{ GeV}^2$. Vertically, \blacktriangle and \bullet are concentrated near $m_{\tilde{L}} = 500 \text{ GeV}$, and there are obvious stratification, from bottom to top are \bullet , \blacktriangle , \blacklozenge . So we can know that as M_{L23}^2 increases, $Br(\tau \rightarrow \mu\gamma)$ increases, and when $m_{\tilde{L}}$ increases, $Br(\tau \rightarrow \mu\gamma)$ decreases. We plot $m_{\tilde{L}}$ varying with T_{e23} in the Fig. 10b. The three types of points are almost symmetrical about $T_{e23} = 0$. The smaller the $m_{\tilde{L}}$ is, the greater the value of $Br(\tau \rightarrow \mu\gamma)$. The farther away the value of T_{e23} from the 0 axis, the greater the value of $Br(\tau \rightarrow \mu\gamma)$. Figure 10c is shown in the plane of T_{e23} versus $m_{\tilde{\nu}_L}$, where the centralized distributions of the three types of points are distributed in a ‘‘U’’ shape on both sides of the $T_{e23} = 0$ axis. \blacklozenge distribute on the innermost side, followed by \blacktriangle and \bullet on the outermost side. So as $m_{\tilde{\nu}_L}$ increases, $Br(\tau \rightarrow \mu\gamma)$ decreases. Finally, we analyze the effects from parameters $\tan \beta$ and $m_{\tilde{L}}$ in Fig. 10d. All points are \blacklozenge , \blacktriangle and \bullet from top to bottom. The smaller the value of $m_{\tilde{L}}$, the larger the value of $Br(\tau \rightarrow \mu\gamma)$.

Table 1 Scanning parameters for Figs. 8, 10 and 11. Without special statement, the non-zero values of non-diagonal elements $m_{Lij}^2, m_{Eij}^2, T_{eij}$ corresponding to $l_j \rightarrow l_i \gamma$ are shown in the column

Parameters/range/processes	$\mu \rightarrow e\gamma (j = 2, i = 1)$	$\tau \rightarrow \mu\gamma (j = 3, i = 2)$	$\tau \rightarrow e\gamma (j = 3, i = 1)$
$\tan \beta$	0.5 ~ 50	0.5 ~ 50	0.5 ~ 50
M_{Lij}^2/GeV^2	0 ~ 5000	0 ~ 5000	0 ~ 5000
M_{Eij}^2/GeV^2	0 ~ 10^4	0 ~ 10^4	0 ~ 10^4
T_{eij}/GeV	-1 ~ 1	-50 ~ 50	-50 ~ 50
$m_{\tilde{\nu}_L}/\text{GeV}$	100 ~ 3000	100 ~ 3000	100 ~ 3000
$m_{\tilde{L}}/\text{GeV}$	400 ~ 2500	400 ~ 2500	400 ~ 2500

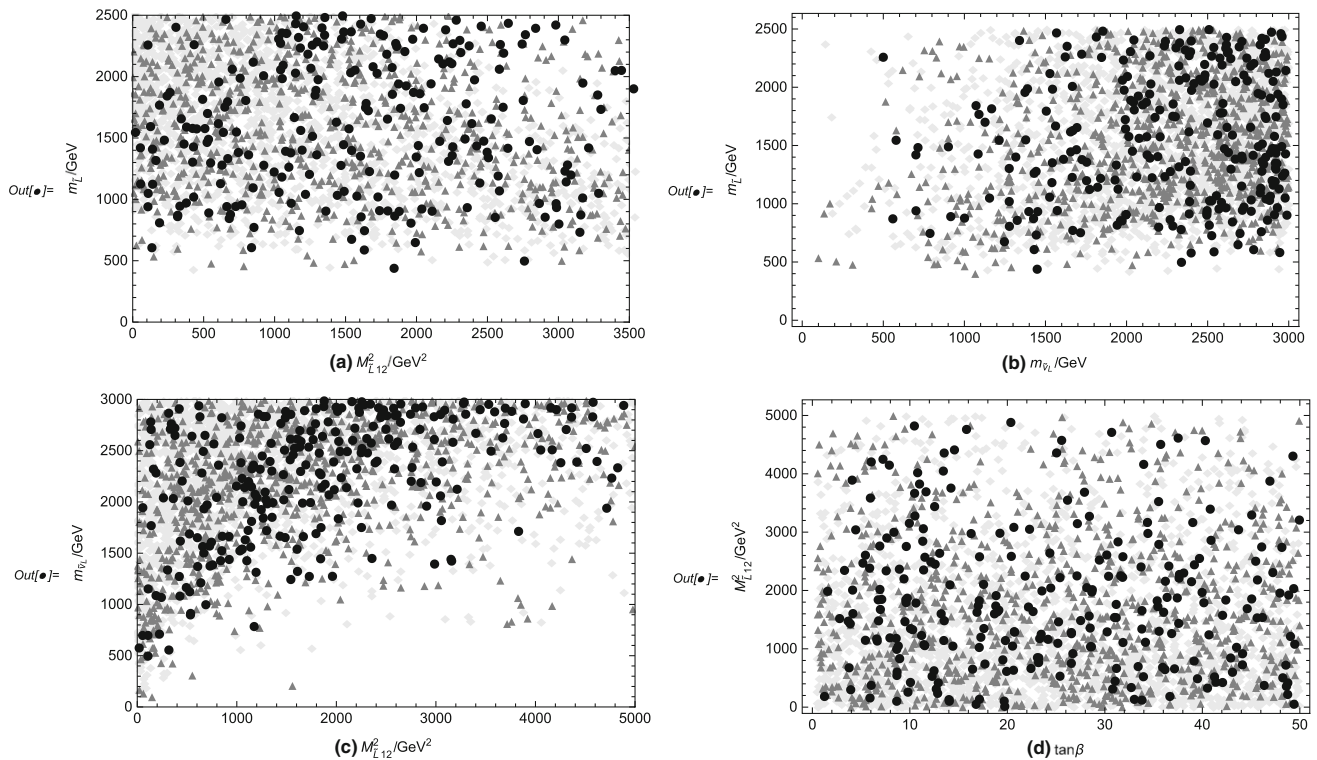


Fig. 8 Under the premise of lower current limit on lepton flavor violating decay $\mu \rightarrow e\gamma$, reasonable parameter space is selected to scatter points, where \blacklozenge mean the value of $Br(\mu \rightarrow e\gamma)$ less than 1.5×10^{-13} ,

\blacktriangle mean $Br(\mu \rightarrow e\gamma)$ in the range of 1.5×10^{-13} to 3.5×10^{-13} , \bullet show $3.5 \times 10^{-13} \leq Br(\mu \rightarrow e\gamma) < 4.2 \times 10^{-13}$

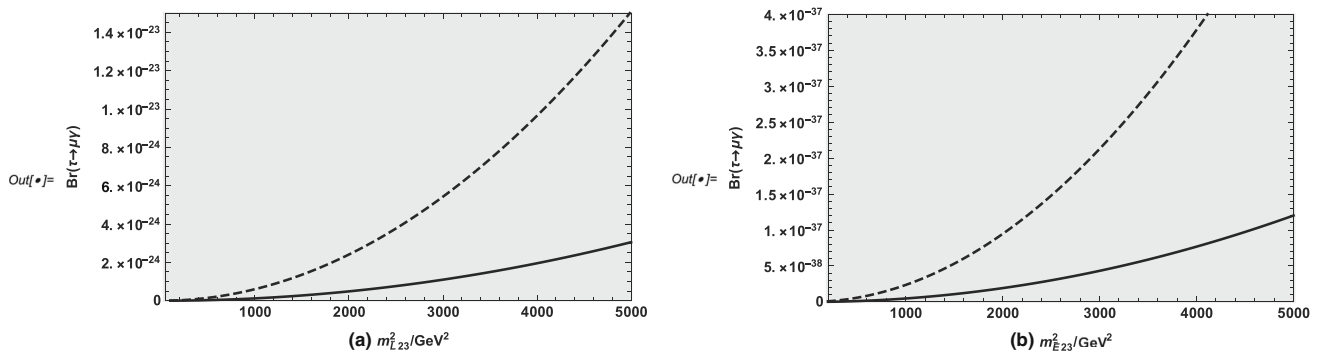


Fig. 9 Below the experimental limit, the line diagram of parameters and $Br(\tau \rightarrow \mu\gamma)$. In **a, b** solid lines and dotted lines represent $\tan \beta = 9$ and $\tan \beta = 20$

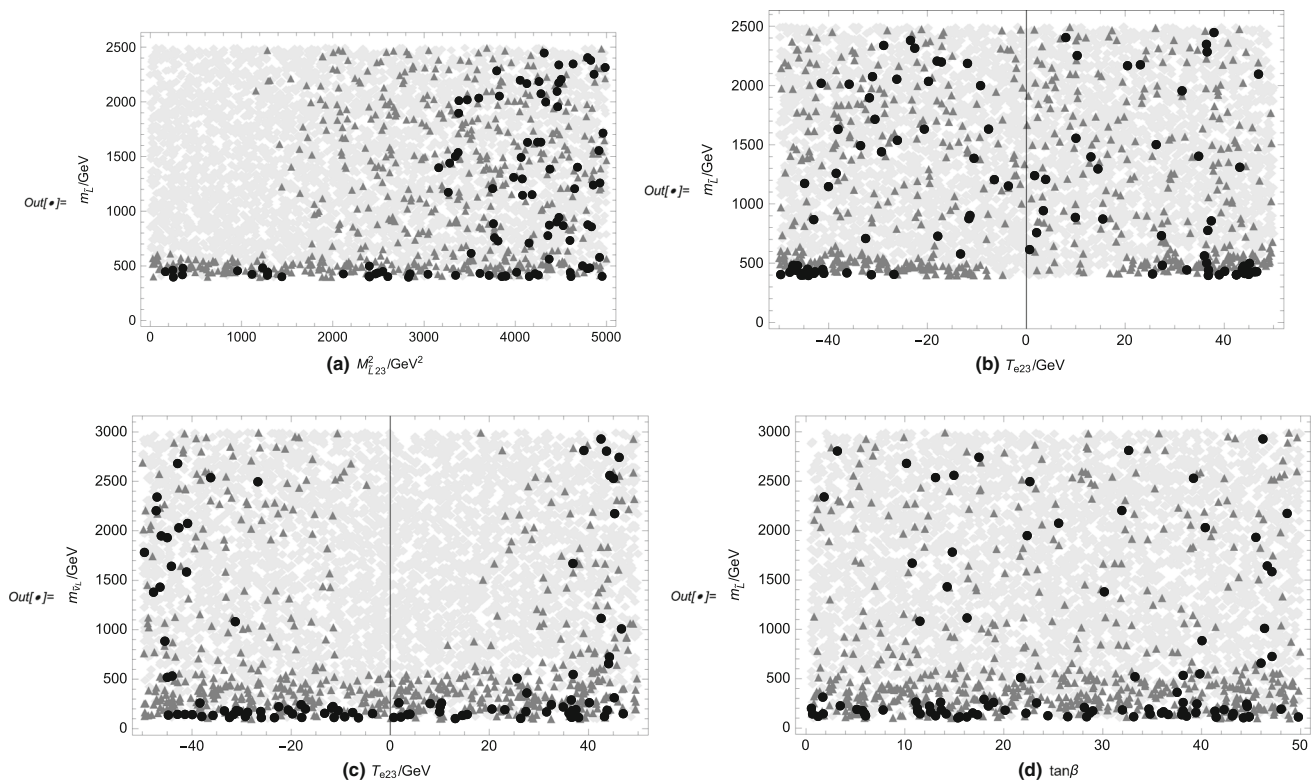


Fig. 10 Scatter points under the restriction of the upper limit of $Br(\tau \rightarrow \mu\gamma)$. \blacklozenge represent $0 < Br(\tau \rightarrow \mu\gamma) < 1 \times 10^{-10}$, \blacktriangle represent $1 \times 10^{-10} \leq Br(\tau \rightarrow \mu\gamma) < 9 \times 10^{-10}$ and $9 \times 10^{-10} \leq Br(\tau \rightarrow \mu\gamma) < 4.4 \times 10^{-8}$ are represented by \bullet

4.4 The processes of $\tau \rightarrow e\gamma$

Based on the Table 1 (part of $\tau \rightarrow e\gamma$), we analyze $\tau \rightarrow e\gamma$ to study the possibility of LFV in Fig. 11. The branching ratio of $\tau \rightarrow e\gamma$ process is denoted by: \blacklozenge ($0 < Br(\tau \rightarrow e\gamma) < 1.0 \times 10^{-10}$), \blacktriangle ($1 \times 10^{-10} \leq Br(\tau \rightarrow e\gamma) < 8.0 \times 10^{-10}$) and \bullet ($Br(\tau \rightarrow e\gamma)$ from 8.0×10^{-10} to 3.3×10^{-8}).

The Fig. 11a shows the effects from $m_{\tilde{\nu}_L}$ and M_{L13}^2 . Most points are concentrated in lower right quarter. \bullet are on the innermost side of the whole region. \bullet are on the innermost side of the whole region. \blacktriangle are in the middle and \blacklozenge are on the outermost side. The numerical performance is that the larger the M_{L13}^2 and the smaller the $m_{\tilde{\nu}_L}$, the larger the $Br(\tau \rightarrow e\gamma)$. In Fig. 11b, we analyze the effects of $m_{\tilde{\nu}_L}$ and $m_{\tilde{L}}$ on $Br(\tau \rightarrow e\gamma)$. In the whole figure, \bullet are mainly close to both sides of the x-axis and y-axis, and then \blacktriangle with the same trend, and the rest is \blacklozenge . $Br(\tau \rightarrow e\gamma)$ decreases with the increase of $m_{\tilde{\nu}_L}$ and $m_{\tilde{L}}$. Figure 11c has two axes $m_{\tilde{L}13}^2$ versus T_{e13} . All three points show “ \supset ” shaped distribution, from left to right are \blacklozenge , \blacktriangle , \bullet . So $Br(\tau \rightarrow e\gamma)$ increases with the increase of T_{e13} .

5 Discussion and conclusion

The $U(1)_X$ SSM has new superfields including right-handed neutrinos and three Higgs superfields $\hat{\eta}$, $\hat{\tilde{\eta}}$, \hat{S} , and its local

gauge group is $SU(3)_C \times SU(2)_L \times U(1)_Y \times U(1)_X$. We use MIA to study muon anomalous magnetic moment. Combined with the latest experimental data, our numerical results can reach about 2×10^{-9} , which can better fit the measurement result, and play a certain role in promoting the study of LFV. We use the method of MIA to study lepton flavor violating decays $l_j \rightarrow l_i\gamma$ in the $U(1)_X$ SSM model. From the order of magnitude of branching ratio and data analysis, we can find that the restriction on lepton flavor violation in the process of $\mu \rightarrow e\gamma$ is stronger. This provides a reference for other lepton flavor violation work in the future.

We take into account the constraints from the upper limits on LFV branching ratios of $l_j \rightarrow l_i\gamma$. In the numerical calculation, we take many parameters as variables including $\tan \beta$, g_X , g_{YX} , $M_{\tilde{L}}^2$, $M_{\tilde{L}ij}^2$, $M_{\tilde{E}}^2$, $M_{\tilde{E}ij}^2$, δ_{ij}^{AB} , $m_{\tilde{L}}$, $m_{\tilde{\nu}_L}$ and T_{eij} . Through the analysis of the numerical results, we find that $M_{\tilde{L}ij}^2$, $M_{\tilde{E}ij}^2$, g_{YX} , δ_{ij}^{AB} , $m_{\tilde{L}}$, $m_{\tilde{\nu}_L}$ and T_{eij} are sensitive parameters. $Br(l_j \rightarrow l_i\gamma)$ is an increasing function of $M_{\tilde{L}ij}^2$, $M_{\tilde{E}ij}^2$, T_{eij} , g_{YX} , δ_{ij}^{AB} , and decreasing function of $m_{\tilde{L}}$ and $m_{\tilde{\nu}_L}$. g_X can also give influence on the numerical results but not very large. That is to say they give mild influences on the numerical results. Finally, we come to the conclusion that the non-diagonal elements which correspond to the generations of the initial lepton and final lepton are main sensitive parameters and LFV sources.

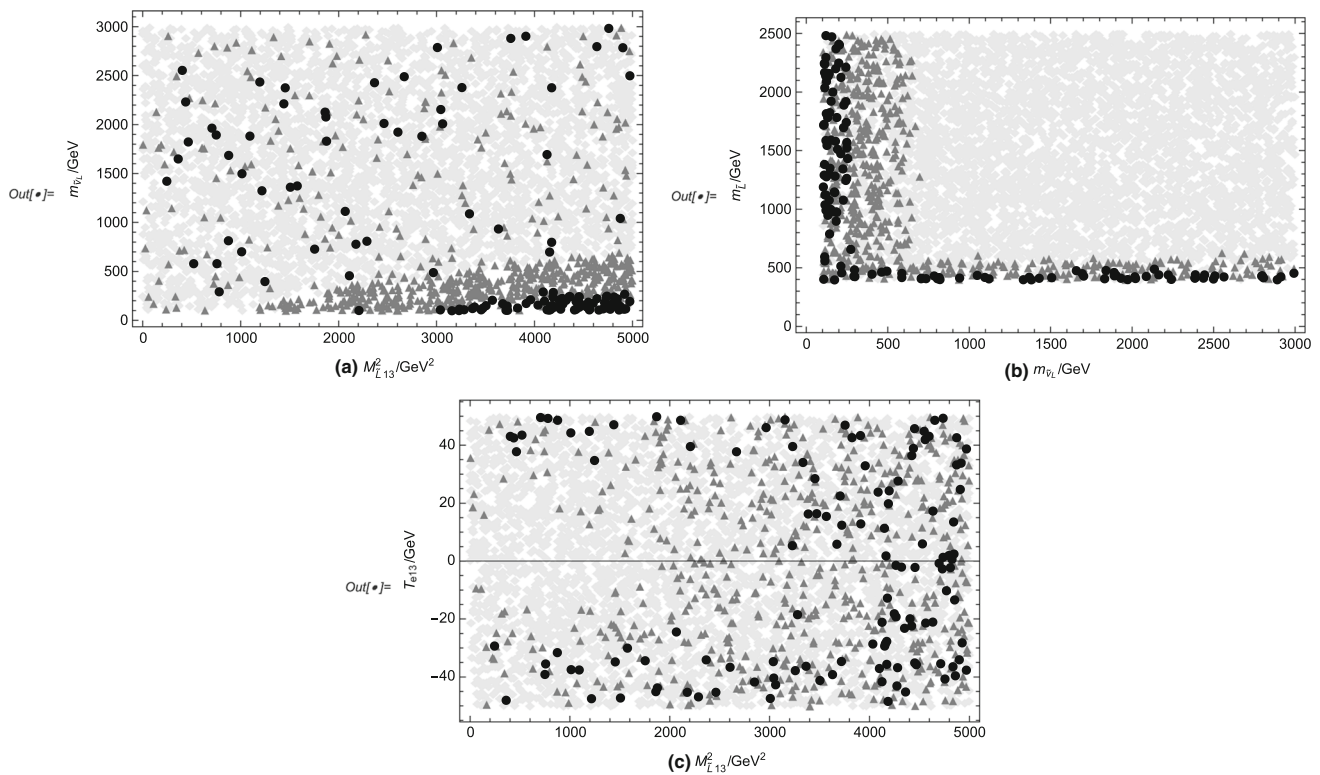


Fig. 11 For the scatter diagrams of the parameters below the experimental limit $Br(\tau \rightarrow e\gamma)$, different points represent the different ranges of $Br(\tau \rightarrow e\gamma)$. \blacklozenge represent less than 1.0×10^{-10} . \blacktriangle represent the range of 1.0×10^{-10} to 8.0×10^{-10} , and \bullet represent the range of 8.0×10^{-10} to 3.3×10^{-8}

Acknowledgements This work is supported by National Natural Science Foundation of China (NNSFC) (no. 11535002, no. 11705045), Natural Science Foundation of Hebei Province (A2020201002). Post-graduate's Innovation Fund Project of Hebei University (HBU2022ss028).

Data Availability Statement This manuscript has no associated data or the data will not be deposited. [Authors' comment: All data included in this manuscript are available upon request by contacting with the corresponding author.]

Open Access This article is licensed under a Creative Commons Attribution 4.0 International License, which permits use, sharing, adaptation, distribution and reproduction in any medium or format, as long as you give appropriate credit to the original author(s) and the source, provide a link to the Creative Commons licence, and indicate if changes were made. The images or other third party material in this article are included in the article's Creative Commons licence, unless indicated otherwise in a credit line to the material. If material is not included in the article's Creative Commons licence and your intended use is not permitted by statutory regulation or exceeds the permitted use, you will need to obtain permission directly from the copyright holder. To view a copy of this licence, visit <http://creativecommons.org/licenses/by/4.0/>.

Funded by SCOAP³. SCOAP³ supports the goals of the International Year of Basic Sciences for Sustainable Development.

References

1. K. Abe et al. (T2K Collaboration), Phys. Rev. Lett. **107**, 041801 (2011)
2. J. Ahn et al. (RENO Collaboration), Phys. Rev. Lett. **108**, 191802 (2012)
3. F. An et al. (DAYABAY Collaboration), Phys. Rev. Lett. **108**, 171803 (2012)
4. S.T. Petcov, Sov. J. Nucl. Phys. **25**, 340 (1977). JINR-E2-10176
5. K.S. Sun, J.B. Chen, X.Y. Yang et al., Chin. Phys. C **43**, 043101 (2019)
6. U. Ellwanger, C. Hugonie, A.M. Teixeira, Phys. Rep. **496**, 1–77 (2010)
7. B. Yan, S.M. Zhao, T.F. Feng, Nucl. Phys. B **975**, 115671 (2022)
8. F. Staub, [arXiv:0806.0538](https://arxiv.org/abs/0806.0538)
9. F. Staub, Comput. Phys. Commun. **185**, 1773 (2014)
10. F. Staub, Adv. High Energy Phys. **2015**, 840780 (2015)
11. J. Rosiek, Phys. Rev. D **41**, 3464 (1990)
12. C.M.S. Collaboration, Phys. Lett. B **716**, 30 (2012)
13. ATLAS Collaboration, Phys. Lett. B **716**, 1 (2012)
14. V. Cirigliano, K. Fuyuto, C. Lee, et al., JHEP **03**, 256 (2021). [arXiv:2102.06176](https://arxiv.org/abs/2102.06176)
15. K.S. Sun, T. Guo, W. Li et al., Eur. Phys. J. C **80**, 1167 (2020)
16. S.M. Zhao, T.F. Feng, H.B. Zhang et al., Phys. Rev. D **92**, 115016 (2015)
17. T. Nomura, H. Okada, Y. Uesaka, Nucl. Phys. B **962**, 115236 (2021)
18. A. Ilakovac, A. Pilaftsis, L. Popov, Phys. Rev. D **87**, 053014 (2013)
19. T.T. Wang, S.M. Zhao, X.X. Dong et al., JHEP **04**, 122 (2022)
20. S.M. Zhao, L.H. Su, X.X. Dong et al., JHEP **03**, 101 (2022)
21. E. Arganda, M.J. Herrero, R. Morales et al., JHEP **03**, 055 (2016)

22. E. Arganda, M.J. Herrero, X. Marcano et al., *Phys. Rev. D* **95**, 095029 (2017)
23. M.J. Herrero, X. Marcano, R. Morales et al., *Eur. Phys. J. C* **78**, 815 (2018)
24. G. Haghightat, M.M. Najafabadi, [arXiv:2204.04433](https://arxiv.org/abs/2204.04433) [hep-ph]
25. Particle Data Group, *Prog. Theor. Exp. Phys.* **2020**, 083C01 (2020)
26. S.M. Zhao, T.F. Feng, M.J. Zhang et al., *JHEP* **02**, 130 (2020)
27. M. Carena, J.R. Espinosa, C.E.M. Wagner et al., *Phys. Lett. B* **355**, 209 (1995)
28. M. Carena, S. Gori, N.R. Shah et al., *JHEP* **1203**, 014 (2012)
29. G. Belanger, J.D. Silva, H.M. Tran, *Phys. Rev. D* **95**, 115017 (2017)
30. V. Barger, P.F. Perez, S. Spinner, *Phys. Rev. Lett.* **102**, 181802 (2009)
31. P.H. Chankowski, S. Pokorski, J. Wagner, *Eur. Phys. J. C* **47**, 187 (2006)
32. J.L. Yang, T.F. Feng, S.M. Zhao et al., *Eur. Phys. J. C* **78**, 714 (2018)
33. T. Moroi, *Phys. Rev. D* **53**, 6565–6575 (1996)
34. C.M.S. Collaboration, *Phys. Lett. B* **716**, 30 (2012)
35. ATLAS Collaboration, *Phys. Lett. B* **716**, 1 (2012)
36. G. Aad et al. (ATLAS), *Phys. Lett. B* **796**, 68–87 (2019)
37. G. Cacciapaglia, C. Csaki, G. Marandella et al., *Phys. Rev. D* **74**, 033011 (2006)
38. M. Carena, A. Daleo, B.A. Dobrescu et al., *Phys. Rev. D* **70**, 093009 (2004)
39. L. Basso, *Adv. High Energy Phys.* **2015**, 980687 (2015)
40. P. Athron, C. Balázs, D.H.J. Jacob et al., *JHEP* **09**, 080 (2021)
41. T. Albahri et al. (Muon g-2), *Phys. Rev. D* **103**, 072002 (2021)
42. M. Endo, K. Hamaguchi, S. Iwamoto et al., *JHEP* **07**, 075 (2021)
43. M. Chakraborti, L. Roszkowski, S. Trojanowski, *JHEP* **05**, 252 (2021)
44. F. Wang, L. Wu, Y. Xiao et al., *Nucl. Phys. B* **970**, 115486 (2021)
45. G.W. Bennett et al. (Muon g-2), *Phys. Rev. D* **73**, 072003 (2006)